STROMAL CELLS

Distinct immunocyte-promoting and adipocyte-generating stromal components coordinate adipose tissue immune and metabolic tenors

Raul German Spallanzani[1], David Zemmour[1], Tianli Xiao[1], Teshika Jayewickreme[1], Chaoran Li[1], Paul J. Bryce[2], Christophe Benoist[1], Diane Mathis[1]*

Regulatory T cells (T_{regs}) are key brakes on the visceral adipose tissue (VAT) inflammation that regulates local and systemic metabolic tenor. Breakdown of this regulation promotes type 2 diabetes. The cytokine IL-33 expands and sustains the unique T_{reg} population residing within VAT. Here, relying on single-cell RNA sequencing, we identified the major IL-33 producers in VAT to be particular mesenchymal stromal cell subtypes, related to but distinct from adipocyte progenitor cells. We explored modulation of the VAT stromal cell landscape with physiologic variables such as age and sex, as well as its remodeling in pathogenic states like obesity. Last, we uncovered a VAT T_{reg}:stromal cell negative regulatory loop that keeps the potent effect of IL-33 under rein.

INTRODUCTION

Innate and adaptive immune system cells exert important positive or negative influences on the sterile inflammation of visceral adipose tissue (VAT) that shapes organismal metabolism (*1*, *2*). VAT-dwelling anti-inflammatory macrophages (*3*, *4*), $Foxp3^+CD4^+$ regulatory T cells (T_{regs}) (*5*), and group 2 innate lymphoid cells (ILC2s) (*6*) are crucial brakes on local inflammation and metabolic dysfunction. In their absence, VAT takes on a pro-inflammatory tenor, and both local and systemic metabolic indices deteriorate, often culminating in type 2 diabetes. Diabetes and its comorbidities are among the 21st century's most important health challenges.

The T_{reg} and ILC2 populations operating within VAT—as well as those functioning in other non-lymphoid tissues—are highly dependent on the cytokine interleukin-33 (IL-33) (*6*–*12*). It is generally agreed that the major source of IL-33 in murine VAT is non-hematopoietic in nature, but there has been debate over its precise identity, with different investigators invoking endothelial cells (*10*) or various phenotypes of fibroblast-like stromal cells (*8*, *13*, *14*). As a paradigm of non-hematopoietic cell control of tissular immune/inflammatory responses, we sought to gain a more profound understanding of the VAT IL-33:T_{reg} axis. To that end, we combined multiparameter flow cytometry, confocal microscopy, genetic ablation, and single-cell RNA sequencing (scRNA-seq) to identify and isolate the critical $IL\text{-}33^+$ cell types in murine VAT; assessed their modulation with normal physiologic variation and with pathologic perturbation; and elucidated an IL-33–focused VAT T_{reg}:stromal cell regulatory loop.

RESULTS

Identification of $IL\text{-}33^+$ cells in murine VAT

To inventorize IL-33–expressing cells in VAT, we prepared a stromal/vascular cut from the epididymal (e)VAT depot of 8- to 10-week-old male C57BL/6 (B6) mice and distinguished four major cell fractions by flow cytometry: $CD45^+$ hematopoietic cells, $CD31^+$ endothelial cells, $PDGFR\alpha^-Sca\text{-}1^-$ double-negative (DN) cells, and $PDGFR\alpha^+Sca\text{-}1^+$ VAT mesenchymal stromal cells (VmSCs) (Fig. 1A). $IL\text{-}33^+$ cells within these fractions were visualized by staining with antibodies (Abs) against podoplanin (PDPN) and IL-33 (intracellularly) (Fig. 1B). Appropriate gating relied on parallel staining of B6 cells with an isotype-control Ab (Fig. 1B, top) and of B6.$Il33^{-/-}$ cells with the anti–IL-33 Ab (Fig. 1C). mSCs were by far the major population of $IL\text{-}33^+$ cells in VAT: About 20 to 40% of $CD45^-CD31^-PDGFR\alpha^+Sca\text{-}1^+$ cells expressed IL-33 above background, and over 90% of IL-33–producing cells fell within this gate (Fig. 1D). Dominant expression of IL-33 by VmSCs was confirmed using an $Il33^{Egfp}$ reporter mouse (fig. S1). Furthermore, mSCs were the major $IL\text{-}33^+$ cells in a range of fat depots: omental (om)VAT, inguinal subcutaneous adipose tissue (iSAT), and brown adipose tissue (BAT) (fig. S2).

Confocal microscopy revealed IL-33–expressing cells at diverse sites in the epididymal fat depot. Many of them localized within a ring of connective tissue at the circumference of the depot, presumably the mesothelium (*15*) (Fig. 1E). [Note that IL-33 is constitutively expressed in the cell nucleus (*16*) and so its staining overlaps with that of 4′,6-diamidino-2-phenylindole (DAPI)]. Other $IL\text{-}33^+$ cells were located in the interior of the depot—often, but not always, in close association with blood vessels (CD31 staining, Fig. 1F) and/or neurons (β3-tubulin staining, Fig. 1G).

Because the identity of the critical $IL\text{-}33^+$ cells in murine VAT has been somewhat contentious, we used conditional knockout mice to confirm the importance of IL-33 expression by $PDGFR\alpha^+$ cells, i.e., mSCs in this context. A mouse strain carrying a "floxed" *Il33* locus was mated with a strain expressing Cre under the dictates of *Pdgfra* promoter/enhancer elements. Offspring that were 12 to 16 weeks old were assayed because this is the age when the eVAT T_{reg} population begins to expand, and thus the proliferation-promoting effects of IL-33 (*7*, *8*) are most likely to be evident. As anticipated, ablation of IL-33 expression specifically in $PDGFR\alpha^+$ eVAT cells had a major impact on whole-tissue *Il33* transcript levels (Fig. 2A), while total VmSC numbers remained unperturbed (fig. S3A). Reflecting the dearth of IL-33, there was a partial diminution of the VAT T_{reg} compartment in eVAT but not iSAT (Fig. 2B). This reduction was similar to that provoked by whole-body ablation of the IL-33 receptor

[1]Department of Immunology, Harvard Medical School and Evergrande Center for Immunologic Diseases, Harvard Medical School and Brigham and Women's Hospital, Boston, MA 02115, USA. [2]Immunology & Inflammation Therapeutic Area, Sanofi US, Cambridge, MA 02139, USA.
*Corresponding author. Email: cbdm@hms.harvard.edu

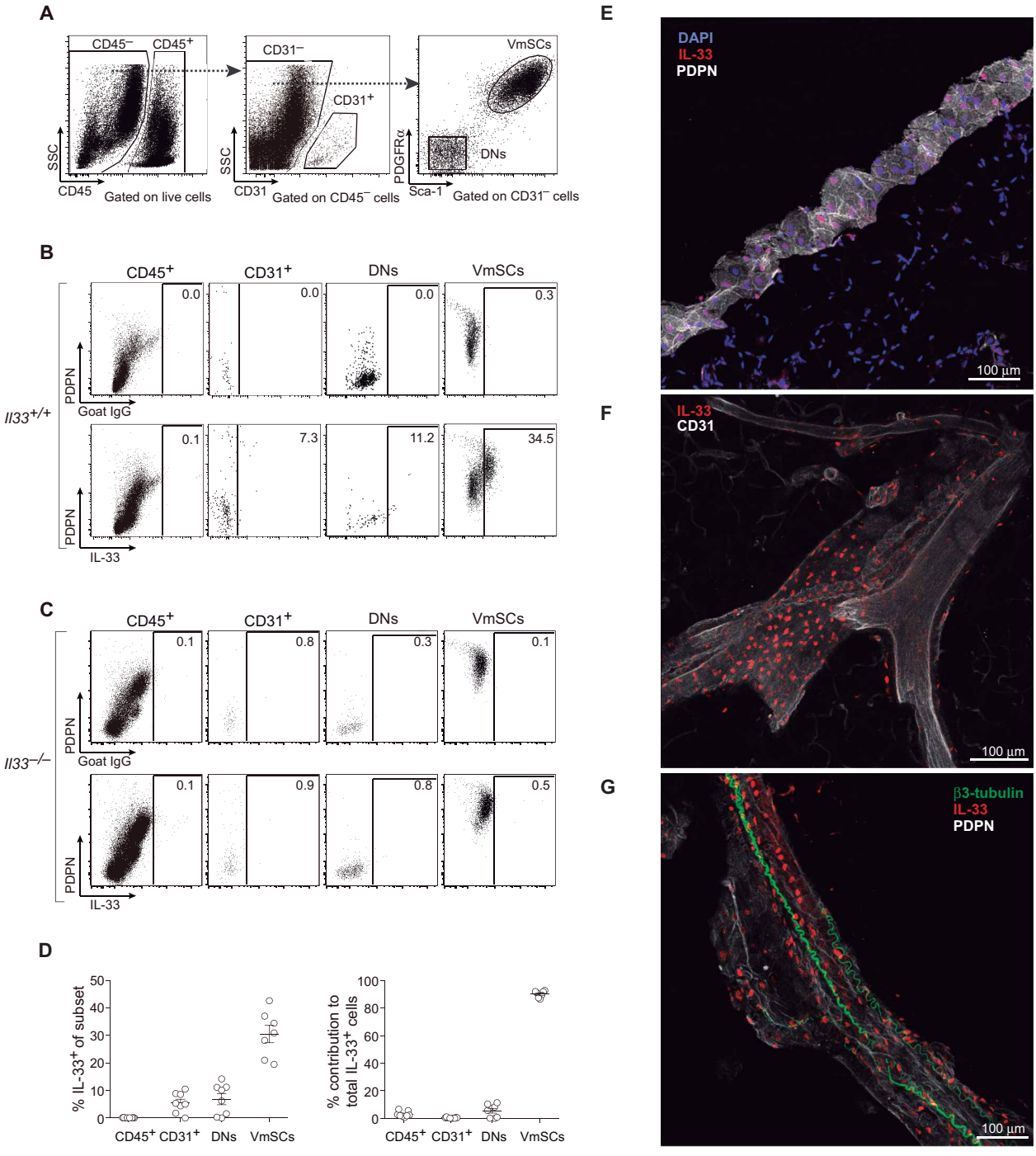

Fig. 1. PDGFRα$^+$Sca-1$^+$mSCs are the main source of IL-33 in eVAT. (**A** to **D**) Cytofluorimetric identification of IL-33–producing cells within eVAT of 8- to 10-week-old B6 mice using a polyclonal anti–IL-33 Ab. (A) Gating strategy to delineate cell fractions. SSC, side scatter. (B) Representative dot plots of control-Ab (top) or anti–IL-33 staining (bottom) of the cell fractions. (C) As per (B) except that whole-body IL-33–deficient (Il33$^{-/-}$) mice were assessed. (D) Frequencies of IL-33$^+$ cells in each cell fraction (left) and its contribution to total IL-33$^+$ cells within the tissue (right). $n \geq 7$ from at least three experiments. (**E** to **G**) Confocal microscopic images of IL-33$^+$ VmSCs. (E) The eVAT depot is bordered by a ring of high PDPN positivity, presumably the mesothelium. (F) IL-33$^+$ cells bordered in close proximity to CD31$^+$ endothelial cells. (G) PDPN positivity outlines a large blood vessel surrounded by β3-tubulin$^+$ nerves. Color code for Ab staining as indicated on top of each picture. PDPN, podoplanin; DNs, PDGFRα-Sca-1$^-$ cells; VmSCs, PDGFRα$^+$Sca-1$^+$ VAT mesenchymal stromal cells.

ST2 encoded by *Il1rl1* (Fig. 2C). In addition, and with both mutations, there were changes in expression of diagnostic eVAT T_{reg} markers: fewer cells expressing ST2, KLRG1, and GATA3, and lower ST2 and KLRG1 mean fluorescence intensities (fig. S3, B to D). There was also a trend toward fewer CD25$^+$ T_{regs} in eVAT, but it did not reach statistical significance (fig. S3E). Also anticipated was that neither the mSC-preferential loss of IL-33 nor the whole-body ablation of ST2 resulted in a difference in body or VAT weight (fig. S3F). Thus,

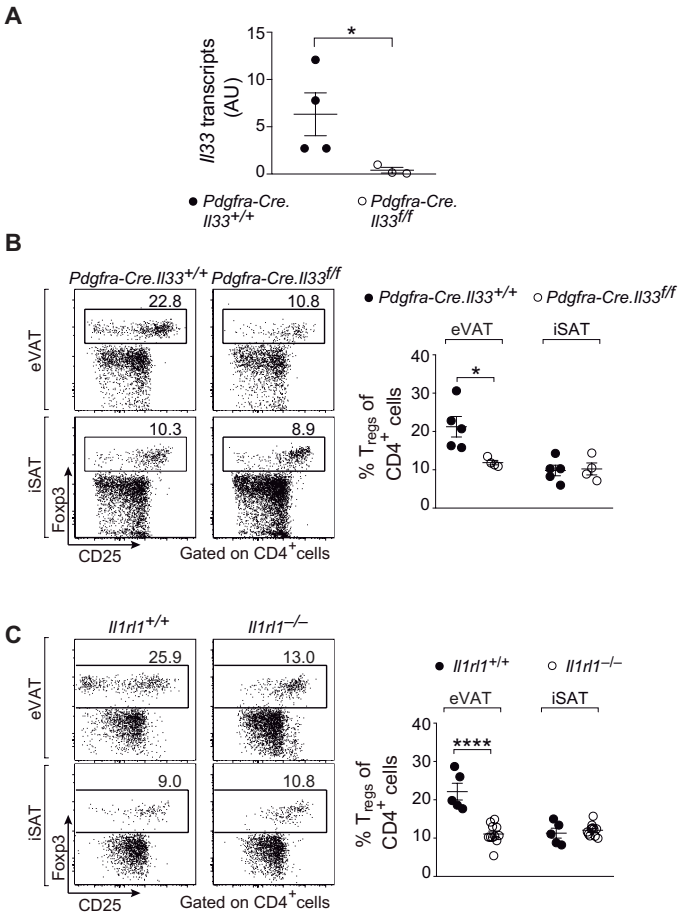

Fig. 2. PDGFRα$^+$Sca-1$^+$mSCs are biologically relevant IL-33 producers. (**A**) Quantitative PCR on whole eVAT of *Il33* transcripts in *Pdgfra-Cre.Il33$^{f/f}$* and corresponding wild-type littermates aged 12 to 16 weeks. (**B** and **C**) Fractions of T_{regs} in *Pdgfra-Cre.Il33$^{f/f}$* (B) and *Il1rl1$^{-/-}$* mice (C) compared with their matching wild-type controls in eVAT (top) and iSAT (bottom). $n \geq 3$ from at least two independent experiments. Mean ± SEM. *$P < 0.05$, ****$P < 0.0001$, according to the one-tailed (A) and two-tailed (B and C) unpaired Student's *t* test. AU, arbitrary units.

PDGFRα$^+$Sca-1$^+$ mSCs were the numerically and functionally important IL-33 expressers in VAT.

mSC heterogeneity in eVAT

PDGFRα$^+$Sca-1$^+$ populations of mSCs have been found in a number of mouse tissues [reviewed in (*17*)]. They have variously been termed fibroblast reticular cells, fibro/adipogenic progenitor cells, mesenchymal stromal cells, or mesenchymal stem cells. They have been attributed a bewildering array of functions: engendering adipocytes, fibroblasts, myocytes, osteoblasts, or chondrocytes; promoting myocyte differentiation from muscle satellite cells; migrating from surrounding adipose tissue to lymph nodes to expand reticular networks; inhibiting inflammation; and, most recently, nurturing local innate and adaptive immunocyte populations. However, it is not known whether all of these functions are exerted by a single cell type or to what extent there is intra- or inter-tissue heterogeneity within the PDGFRα$^+$Sca-1$^+$ population.

To address these points, we performed scRNA-seq on cytofluorimetrically sorted CD45$^-$CD31$^-$PDGFRα$^+$Sca-1$^+$PDPN$^+$ populations from eVAT, skeletal muscle, and pooled lymph nodes of 8- to 10-week-old B6 mice using the InDrops protocol (*18*). In total, 3720 individual cells were analyzed; on average, 3926 unique mRNA molecules transcribed from 1513 different genes were sequenced per cell. We first displayed the combined data as a t-distributed stochastic neighbor embedding plot, permitting dimensionality reduction. Substantial intra- and inter-tissue heterogeneity was evident: Each tissue hosted five to seven mSC subtypes, which grouped largely according to tissue source (Fig. 3A). Unsupervised transcript clustering revealed the five VmSC subtypes to have readily distinguishable transcriptomes, with a distinct cluster of overrepresented transcripts for each subtype plus three more complex clusters (Fig. 3B and table S1). Unexpectedly, velocity analysis, which predicts differentiation pathways based on the ratio of spliced to unspliced introns in the totality of mRNAs (*19*), failed to reveal clear vectors of differentiation between the various VmSC subtypes (Fig. 3C), suggesting that they are likely to be independent entities whose transcriptomes have converged to some degree in response to local cues. As anticipated from the sorting strategy, all five VmSC subtypes expressed *Pdgfra* and *Ly6a* (encoding Sca-1) transcripts, though at variable frequencies (Fig. 3D, left). VmSC1 to VmSC3 were the primary *Il33*-expressing subtypes, while *Pparg* transcripts, characteristic of adipocytes and their immediate precursors, showed a reciprocal pattern of expression [Fig. 3, D (middle) and E].

Mining of the transcriptomic data suggested a strategy for cytofluorimetric sorting of the individual VmSC subtypes based on *Il33*, *Pparg*, *Thy1*, and *Cd55* transcript levels [Fig. 3, D (right) and E]. Combining fluorescent reporters of peroxisome proliferator–activated receptor γ (PPARγ) and/or IL-33 expression (described in Supplementary Materials and Methods) with Abs recognizing Thy1 and CD55 did permit isolation of the individual subtypes (Fig. 3F and fig. S4). This was an important advance because it allowed validation of the VmSC subtypes defined via scRNA-seq analysis, enabled a deeper phenotypic comparison of these cell populations, and facilitated rapid, cost-effective evaluation of their modulation in diverse physiologic states.

As concerns validation, the relative proportions of the five VmSC subtypes defined according to single-cell transcriptomics and those delineated by cytofluorimetric assessment of marker expression were similar, as were their IL-33 expression levels (as long as mice of the same sex, age, and husbandry were analyzed) (Fig. 3, F and G). In addition, Spearman correlation analysis of the genes differentially expressed ≥2-fold in the five VmSC scRNA-seq datasets showed a strong correspondence with population-level RNA-seq datasets derived from the analogous cytofluorimetrically sorted VmSC subtypes (Fig. 3H).

Functional features of the VmSC subtypes

The deeper sequencing coverage afforded by population-level analysis of the individual VmSC subtypes uncovered several additional points of interest. First, all five subtypes expressed high levels of transcripts encoding the pan-fibroblast markers collagen1a2, vimentin, and collagen3a1 (Fig. 4A). Second, principal component analysis (PCA) showed VmSC2 to be the most divergent of the five populations (Fig. 4B), consistent with the fact that VmSC2 had more genes ≥2-fold up- or down-regulated vis-à-vis the four other subtypes than did VmSC1 and VmSC3 to VmSC5 (>1100 versus <900). Third, Gene Set Enrichment Analysis (GSEA) revealed an overrepresentation of the "epithelial-mesenchymal transition" pathway, a hallmark of tissue remodeling and fibrosis, in VmSC1 and VmSC2, whereas

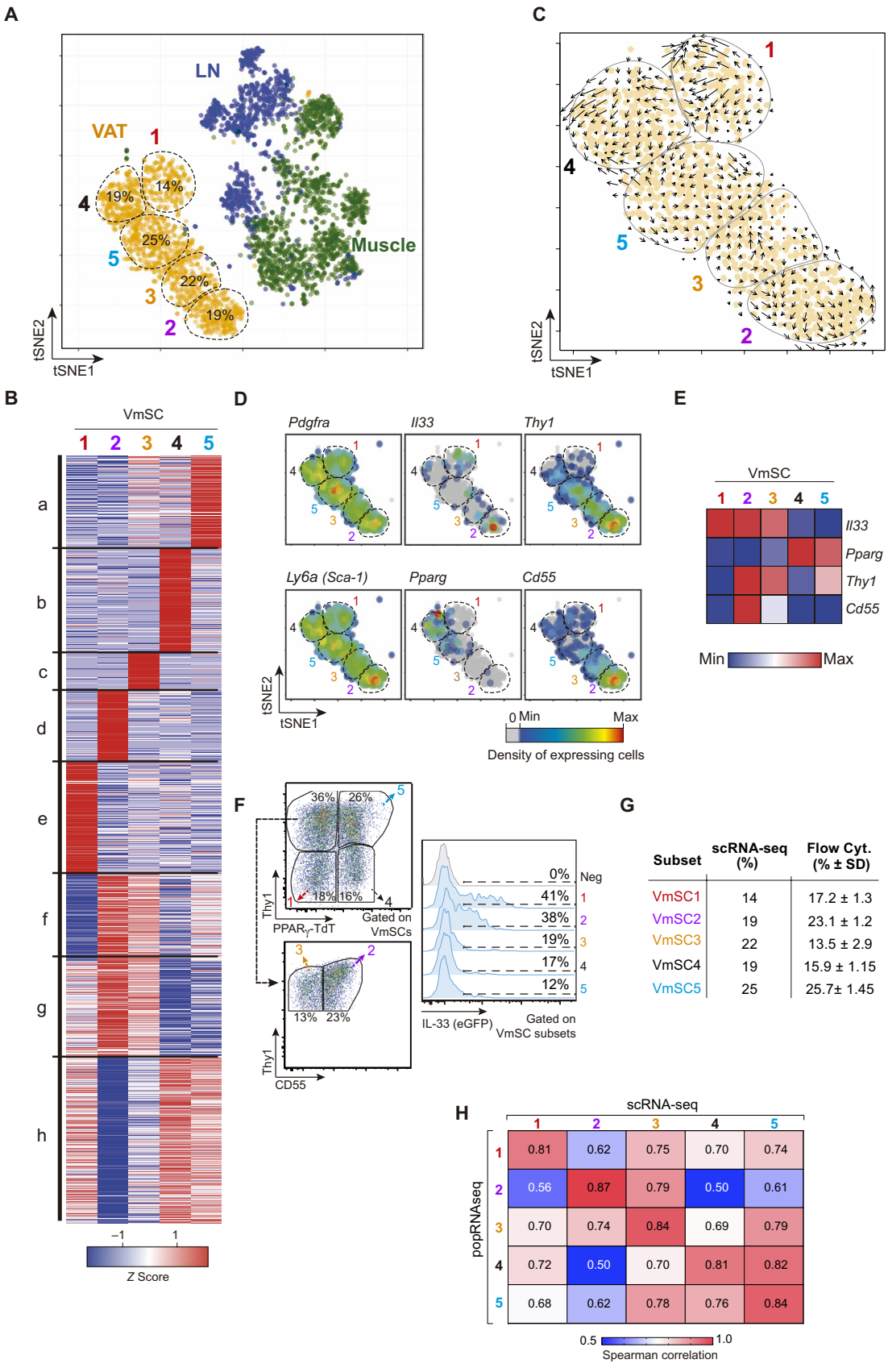

Fig. 3. mSCs exhibit extensive transcriptional heterogeneity. (**A**) Two-dimensional t-distributed stochastic neighbor embedding (tSNE) plot of scRNA data from VAT (orange), muscle (green), and lymph node (blue) PDGFRα^{+}Sca-1^{+} mSCs. VmSC subtypes 1 to 5 were delineated by k-means clustering; their fractional contributions to total VmSCs are indicated. (**B**) Heatmap showing genes differentially expressed between the VmSC subtypes [false discovery rate (FDR) < 5%]. k-means clustered. (**C**) VmSC dynamics (velocity field). The projected next cell state for each single cell is represented by an arrow and projected on the tSNE plot. (**D**) Same tSNE plot as in (A) overlain with heatmaps of the density of cells expressing various transcript markers. (**E**) Heatmap of transcript expression within the combined single-cell data of each VmSC subtype. (**F**) Representative dot plots delineating the VmSC subtypes (left) and indicating their IL-33 expression levels (right) in Pparg^{Tdt}Il33^{Egfp} double-reporter mice. TdT, TdTomato; eGFP, enhanced green fluorescent protein. (**G**) Comparison of VmSC subtype frequencies obtained by scRNA-seq versus flow cytometry. (**H**) Matrix of Spearman correlation coefficients in head-to-head comparisons of ≥2-fold differentially expressed genes from the scRNA-seq and matching population (pop)-level RNA-seq datasets. LN, lymph node.

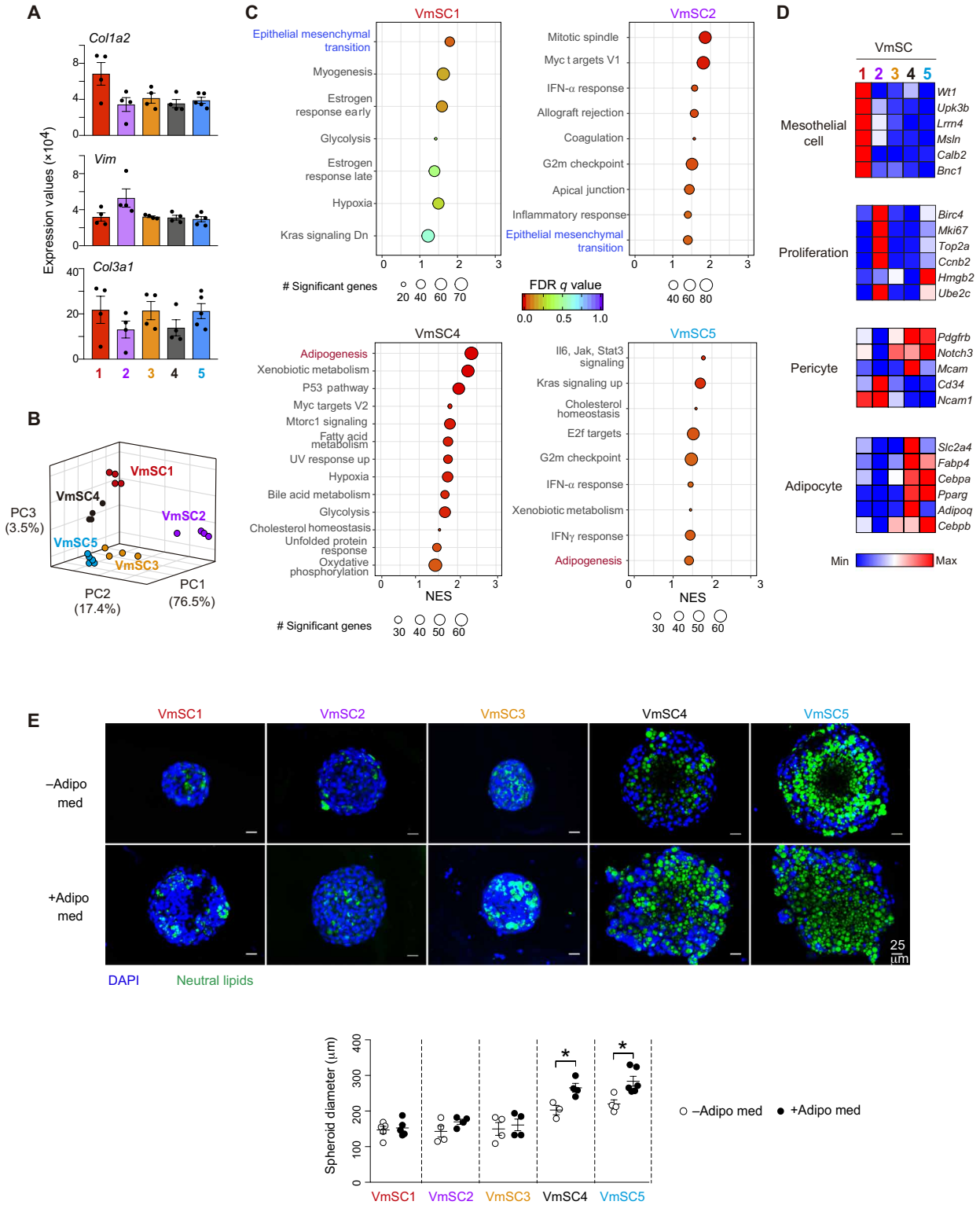

Fig. 4. mSC subtypes exhibit different functional properties. (**A**) Gene expression of pan-fibroblast genes across VmSC populations. (**B**) Three-dimensional PCA plot depicting the VmSC subsets. (**C**) GSEA-derived hallmarks for individual VmSC subtypes compared with the rest. The size of the circles denotes the number of genes significantly enriched in each individual pathway; rainbow color code indicates FDR values, and NES (normalized enrichment score) is depicted on the *x* axis of the plot. IFN-α, interferon-α. (**D**) Expression heatmaps for transcripts considered cardinal for the indicated cell types. All should be overexpressed, except *Cd34* and *Ncam1*, which were underexpressed in pericytes. Precise expression values appear in table S3. (**E**) Representative images of three-dimensional in vitro cultured VmSCs in the absence (–) or in the presence (+) of an adipogenic medium (Adipo med) (top). Quantification of the spheroid diameter (bottom). All data from 8- to 10-week-old males of B6 genotype unless indicated otherwise. *$P < 0.05$. GSEA pathways were filtered based on a *P* nominal value <0.05. Other abbreviations as per Fig. 1.

VmSC4 and VmSC5 showed enrichment for the "adipogenesis" pathway (Fig. 4C and table S2). Fourth, analysis of cardinal marker transcripts (*20*) indicated that VmSC subtype 1 had a clear mesothelial component (Fig. 4D, top, and table S3) and was thus likely to encompass the population of IL-33$^+$ cells at the circumference of the epididymal fat pad (Fig. 1E). Consistent with the GSEA analysis, VmSC2 was enriched for transcripts encoding markers of proliferation (Fig. 4D, upper middle), perhaps driving its strong divergence from the other four subtypes. VmSC4 and VmSC5 exhibited the pattern of cardinal transcript overexpression (*Pdgfrb*, *Notch3*, and *Mcam*) and underexpression (*Cd34* and *Ncam1*) expected of pericytes or mural cells (Fig. 4D, lower middle, and table S3) (*20*). (Note that subtypes 1 and 3 also showed pericyte signatures, but more weakly, likely corresponding to the vascular IL-33$^+$ cells depicted in Fig 1F.) VmSC4 and VmSC5 exhibited the strongest expression of diagnostic adipocyte transcripts as well, with VmSC4 seeming to be the more mature of the two cell types (Fig. 4D, bottom, and table S3).

Hence, VmSC subtypes 4 and 5 had phenotypes highly reminiscent of a recently identified mural cell adipocyte precursor residing in murine VAT (*21*), concordant with results from a three-dimensional in vitro assay of their adipogenic potential. Sorted VmSC4 and VmSC5 populations, but not the IL-33$^+$ VmSC subtypes, robustly responded to culture in adipogenic medium by enlarging and accumulating neutral lipids in the cytoplasm; actually, these characteristics were already evident, if muted, without adipogenic stimuli (Fig. 4E). VmSC4 and VmSC5 (as well as the other VmSC subtypes) did not express high levels of most adipokines at steady state (fig. S5A), as expected of their immature state. Last, the differential expression of extracellular matrix proteins (fig. S5B and table S4) and soluble mediators (fig. S5C and table S4) reinforced the notion of VmSC subtype heterogeneity. Note, for example, the particularly low expression of genes encoding extracellular matrix proteins by VmSC2. Thus, the picture that emerged was one of heterogeneous functional potential: an IL-33–producing subtype (VmSC1) that had a mesothelial component, another IL-33–producing subtype (VmSC2) that was proliferating, two *Pparg*-expressing subtypes (VmSC4 and VmSC5) that could engender adipocytes, and a subtype (VmSC3) that was difficult to pigeonhole.

VmSC subtype evolvement with physiologic variation: T_{reg}:VmSC1 to VmSC3 correlations

Next, we exploited the marker panel to assess modulation of the five VmSC subtypes with normal physiologic variation. Concordant with previous reports (*5*, *8*, *22*), there were significant increases in the fraction and number of eVAT T_{regs} as male B6 mice matured from 6 to 32 weeks of age, particularly for the "true" eVAT-phenotype subpopulation expressing elevated levels of ST2 and GATA3 (fig. S6A) (*8*), paralleling rises in body and fat-pad weights (fig. S6B). There was also an enrichment in total (Fig. 5A) and IL-33$^+$ (Fig. 5B) VmSCs as the mice aged, especially in numbers of VmSC1 to VmSC3 (Fig. 5, C and D).

Female gonadal (g)VAT, i.e., ovarian (o)VAT, does not show the enrichment in T_{regs} typical of eVAT in males (*9*). The root of this divergence remains entirely unknown. Whether mice were 18 to 20 (fig. S7A) or 8 to 10 (fig. S7B) weeks old, we were able to recapitulate this difference and to add that it applied to true gVAT T_{regs} enriched in cells expressing high levels of ST2 and GATA3. In contrast, there were no significant differences in T_{reg} fractions or numbers in male and female iSAT depots (fig. S7, A and B). As in eVAT, the vast majority of IL-33–expressing cells in oVAT were PDGFRα$^+$Sca-1$^+$ mSCs (fig. S8A), as was also the case in female omVAT, iSAT, and BAT depots (fig. S8B). Of note, oVAT in all females examined contained two cell populations with phenotypes hardly observed in eVAT: PDGFRα$^+$Sca-1$^-$ and PDGFRα$^-$Sca-1$^+$ cells; however, these cells expressed few or no *Il33* transcripts (fig. S8, A and B). At both ages, but especially in older individuals, there were more IL-33$^+$ mSCs in the male than in the female gVAT depot (Fig. 6A and fig. S8C). There was also a very different stromal landscape in the two sexes: more VmSC1, VmSC3, and VmSC4 in males, coupled with fewer VmSC5 (Fig. 6B and fig. S8D). To determine whether the reduction in gVAT T_{regs} in female mice might reflect limiting IL-33 levels, we injected 8- to 10-week-old females twice with IL-33 and examined T_{reg} levels and phenotype 6 days after the initial injection. There was a strong increase in the fraction and number of T_{regs} in oVAT in response to IL-33 injection (fig. S8E), attaining levels at least as high as those observed for eVAT at steady state (fig. S7A). The increase was also true of ST2$^+$, KLRG1$^+$, and GATA3$^+$ T_{regs}, in particular (fig. S8F).

Although the dearth of IL-33$^+$ mSCs in female gVAT might explain the defect in local T_{reg} accumulation, we performed head-to-head comparative transcriptomics for additional insights. PCA revealed similar intra-sex clustering patterns for the five VmSC subtypes; however, for each subtype, the male and female transcriptomes clustered apart, largely along a single axis, PC2 (Fig. 6C). Pairwise comparisons highlighted the "fatty acid metabolism" pathway in all cases and early and/or late "estrogen response" pathways in all but the VmSC2 subtype (table S5). *Esr1* transcripts, encoding the estrogen receptor, were much more highly expressed in all female than in male VmSC subtypes (Fig. 6D). Such a gender difference in *Esr1* transcription was not a foregone conclusion—for example, it is not seen with a diversity of immunocyte populations (www.immgen.org). *Ar* transcripts, encoding the androgen receptor, were also increased in the VmSC1 and VmSC2 populations of females (Fig. 6D).

Meta-analysis of the aging and gender results, i.e., all of the data from normal physiologic states, revealed highly significant correlations between numbers of ST2$^+$ T_{regs} and VmSC numbers for each of the IL-33–expressing subtypes, above all for VmSC1 (Fig. 6E). In contrast, there was no correlation with VmSC4 and VmSC5 numbers. This observation reinforces the notion of divergent VmSC subtypes primarily dedicated to promoting immunocytes versus generating adipocytes.

VmSC subtype evolvement with pathogenic perturbation: IL-33–mediated T_{reg}:VmSC cross-talk

To determine whether and how VAT stroma is remodeled under pathogenic conditions, i.e., obesity, we exposed 14-week-old B6 male mice to a high-fat diet (HFD) for 4 (short term) or 16 (long term) weeks. As anticipated (*5*), the metabolic abnormalities induced by long-term HFD feeding (fig. S9, A and B) were accompanied by a notable reduction in the VAT T_{reg} compartment, and the few remaining cells had a less VAT-like (i.e., less ST2$^+$) phenotype (fig. S9C). Total and IL-33–expressing VmSCs were reduced shortly after introduction of the HFD, but by 16 weeks they had bounced back to supraphysiologic levels (Fig. 7A and fig. S9D). There was also major remodeling of the VmSC subtype landscape with prolonged HFD feeding, most notably an enrichment in the numbers

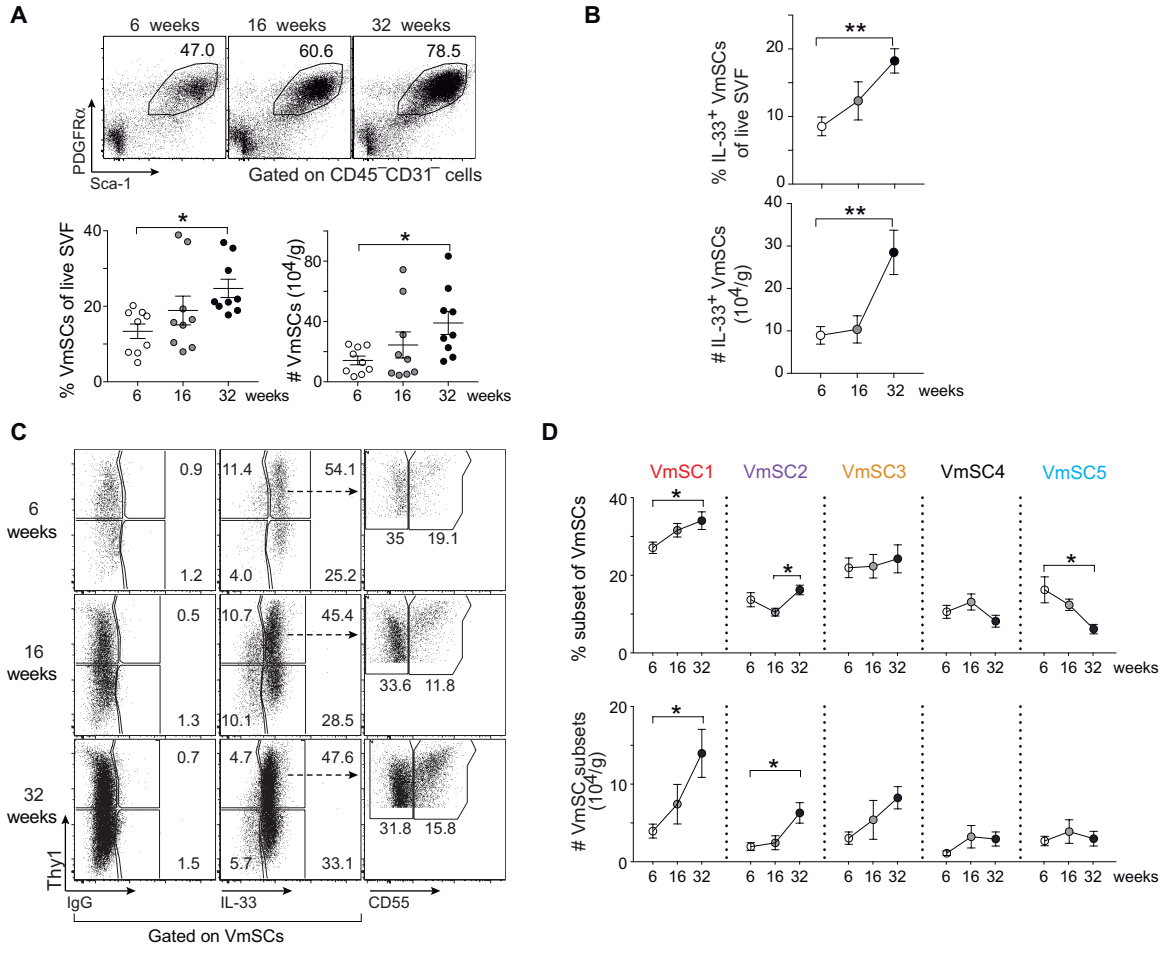

Fig. 5. Age strongly influences immunocyte-promoting VmSCs and thereby T_{reg} accumulation. (**A**) Representative plots (top) and frequencies and numbers (bottom) of total VmSCs from mice of different ages. (**B**) Frequencies (top) and numbers (bottom) of total IL-33$^+$ VmSCs. (**C** and **D**) Cytofluorometric dot plots of VmSC subtypes (C) and corresponding fractions (top) and numbers (bottom) (D) from lean B6 males of the indicated ages. Pooled data from three independent experiments. Numbers of cells were normalized per tissue weight. One-way ANOVA analysis was performed to compare three or more groups. For all relevant plots, mean ± SEM. *$P < 0.05$, **$P < 0.01$. SVF, stromal vascular fraction. Other abbreviations as per Fig. 1.

of all three IL-33$^+$ subtypes (fig. S9E and Fig. 7B). Transcriptome analysis indicated that this grouping is probably equivalent to the profibrotic PDGFRα$^+$CD9$^+$ subset of mouse and human VAT stromal cells recently reported to expand with obesity (*23*) (table S1, cluster g).

Thus, the positive correlation between VAT T_{reg} numbers and IL-33$^+$ VmSC subtype numbers broke down in HFD-induced obesity. An explanation for this observation might be that VAT T_{regs} normally keep IL-33–expressing stromal cells in check, in a negative feedback loop. HFD-induced defects in the size or phenotype of the VAT T_{reg} compartment, as have been documented (*5*, *7*, *22*, *24*), might thereby unleash VmSC1 to VmSC3. To test the possibility of IL-33 participation in such a VAT T_{reg}:VmSC regulatory loop, we twice injected this cytokine, 3 days apart, into 10-week-old B6 males, and we analyzed them 6 days after the initial injection. There was no significant increase in the fraction or number of total VmSCs expressing IL-33 in response to this acute treatment (Fig. 7C), but there was substantial remodeling of the subtype landscape, particularly a large relative decrease in the VmSC1 compartment with a concomitant strong increase in VmSC5 (Fig. 7D).

Because the mSCs in VAT do not express *Il1rl1* transcripts, encoding ST2, at levels significantly above background (≤4), we surmised that the alterations in VmSC subtype distribution were due to indirect effects via another cell type. T_{regs} and ILC2s express the highest levels of ST2 in VAT, and injection of IL-33 expanded both of these lymphocyte subsets in this context (Fig. 8, A and B). Given the ready availability of more specific reagents, particularly knockout mice, we focused on the contribution of T_{regs} but do not rule out additional participation by ILC2s, the focus of an accompanying paper (*25*). Frequent proximity (≤50 μm) between T_{regs} and IL-33$^+$ stromal cells was demonstrated by confocal microscopy of eVAT from mice with an enriched VAT T_{reg} compartment (*9*) for ease of visualization (Fig. 8C). More importantly, injection of IL-33 into mice lacking ST2 specifically on T_{regs}, in comparison with parallel injections into wild-type littermates, showed muted expansion of the VAT T_{reg} population, particularly the true VAT-phenotype KLRG1$^+$ component (Fig. 8D) (*8*); actually enhanced expansion of the ILC2 compartment (Fig. 8E); and allowed a greater increase in total IL-33$^+$ VmSCs (Fig. 8F), especially in subtypes 2 and 3 (fig. S10). Together,

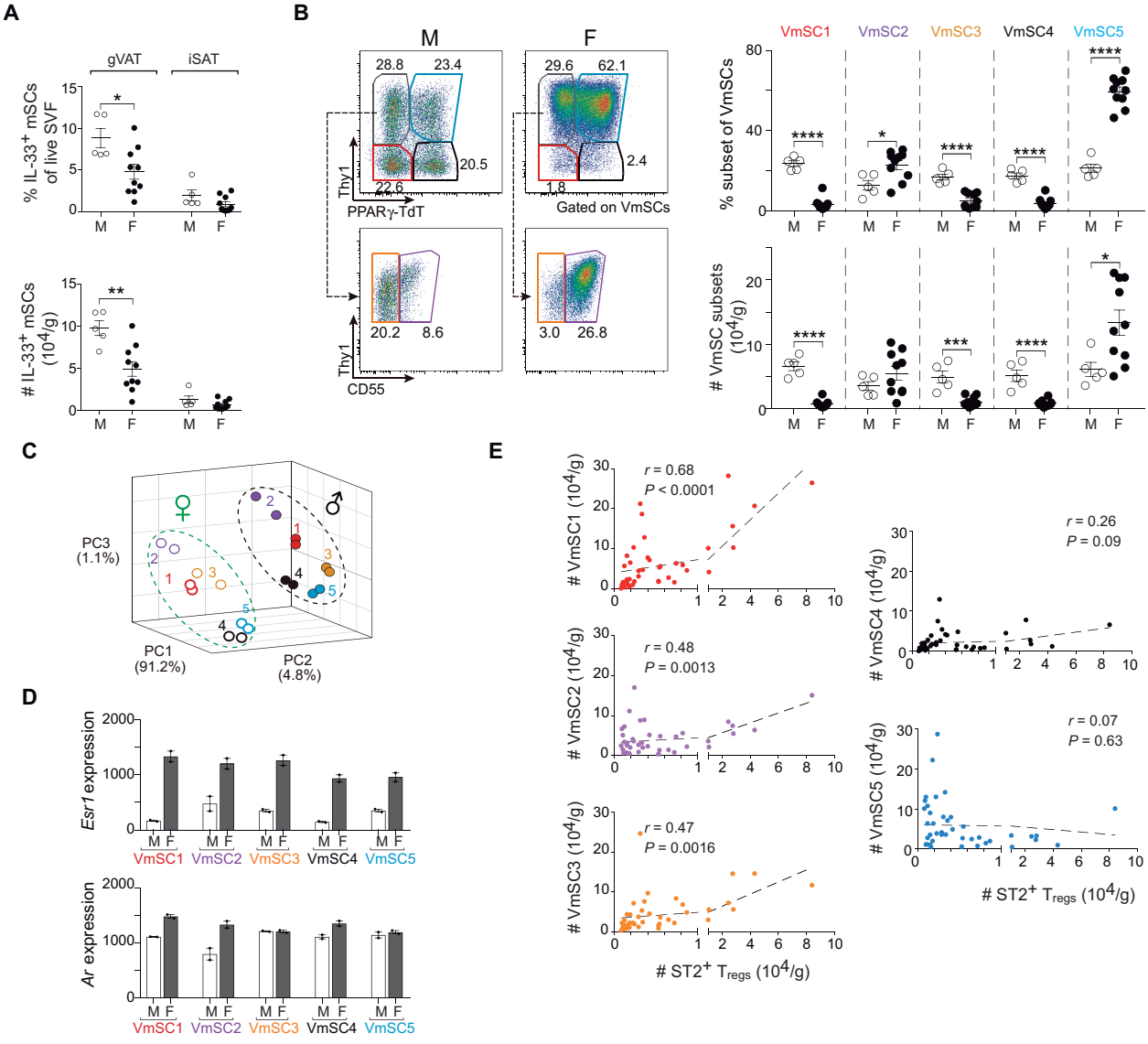

Fig. 6. Gender determines drastically distinct VmSC subtype distribution and VAT T_{reg} abundance. (**A**) Frequencies (top) and numbers (bottom) of total IL-33$^+$ VmSCs. (**B**) Cytofluorimetric dot plots (left) and corresponding quantification of subtypes thereof (right) in gVAT and iSAT of lean male (M) and female (F) mice aged 18 to 20 weeks old. Pooled data from at least two independent experiments. (**C**) Three-dimensional PCA plot of the transcriptomes (population-level RNA-seq) from coincidently prepared male and female VmSC subtypes from B6 mice 8 to 10 weeks old. (**D**) *Esr1* (top) and *Ar* (bottom) transcripts levels for the individual VmSC subtypes from male (white bars) and female (black bars) mice aged 8 to 10 weeks old. Each dot represents an individual biological replicate from two or more pooled mice. *$P < 0.05$, **$P < 0.01$, ***$P < 0.001$, ****$P < 0.0001$. (**E**) Correlation curves for numbers of IL-33$^+$ VmSCs versus ST2$^+$ T_{reg} numbers in gVAT using metadata from all male mice of various ages (6, 16, 18 to 20, and 32 weeks) and female mice 18 to 20 weeks old, i.e., all mice of normal physiologic state. In all cases, numbers of cells were normalized to tissue weight. *r* and *P* from Pearson's correlation coefficient. All other statistics and abbreviations as per Figs. 1 and 5.

then, the data on obese mice and IL-33–injected wild-type and ST2-deficient mice point to a control loop wherein VAT ST2$^+$ T_{regs}, expanded and sustained by IL-33 in normal physiologic states, negatively regulate IL-33–expressing VmSCs; this loop breaks down in the obese state, with its compromised VAT T_{reg} compartment (Fig. 8G).

DISCUSSION

Our results highlight mSCs as key orchestrators of metabolic: immunologic cross-talk in adipose tissue. This stromal compartment turns out to be very heterogeneous, both within and between tissues. In healthy individuals, dedicated VAT mSC subtypes coordinately balance immunocyte numbers through secretion of IL-33 (VmSC1 to VmSC3) and adipocyte numbers/activities through regulation of adipocyte precursors (VmSC4 and VmSC5). Remodeling of the VmSC landscape associated with disease states such as obesity [and probably infection (*26*)] destroys this harmony, resulting in metabolic and/or immunologic aberrancies. For example, T_{regs} are unable to accumulate in VAT of obese mice (*5*), likely reflecting modulation of PPARγ activity (*22*, *24*), and thus cannot rein in accumulation of and IL-33 production by VmSC1 to VmSC3 as they

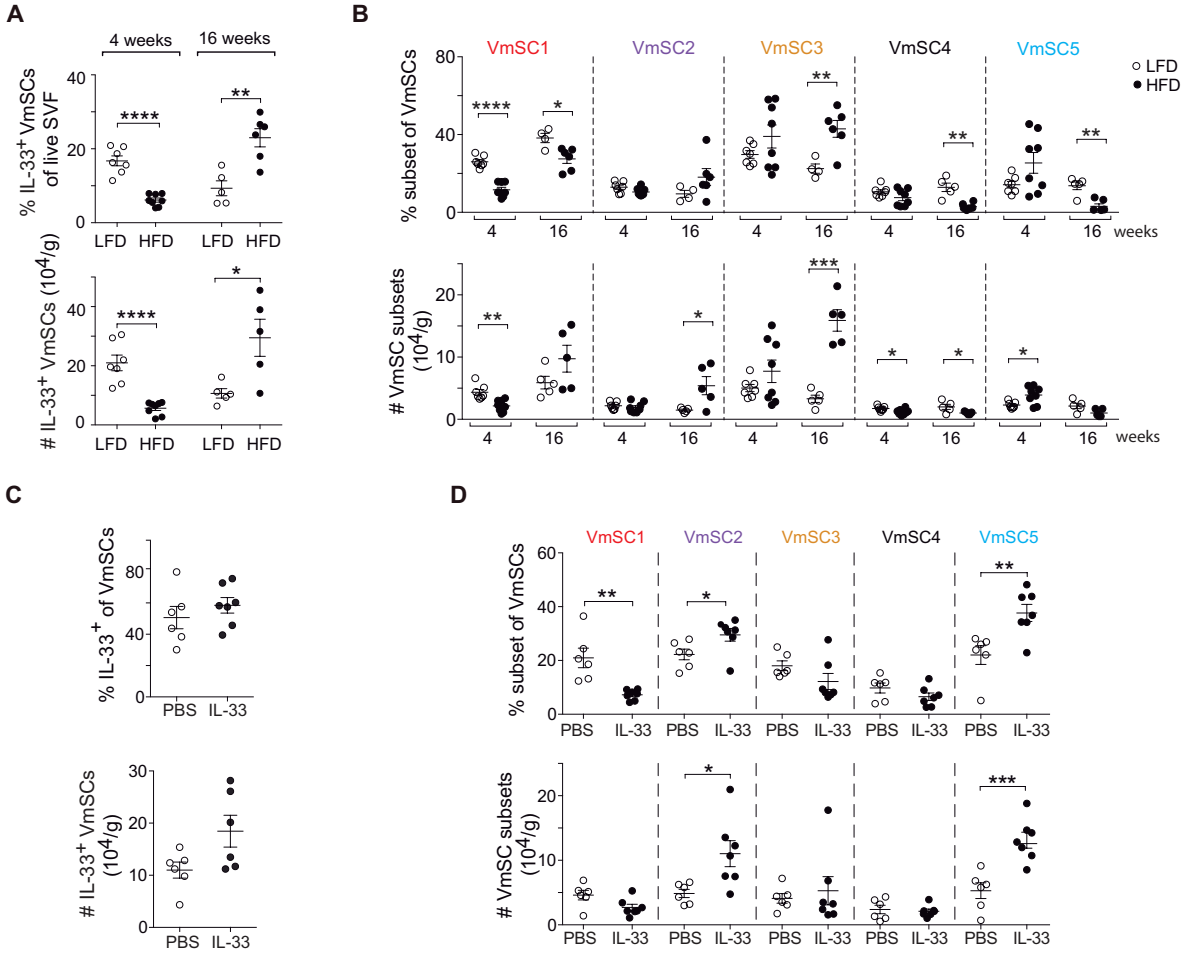

Fig. 7. An IL-33–focused VAT T_{reg}:VmSC regulatory loop is uncovered in obese mice. (**A** and **B**) Fractions (top) and numbers (bottom) of total IL-33$^+$ VmSCs (A) and VmSC subtypes (B) subsequent to 4 or 16 weeks of high-fat feeding of 14-week-old B6 males. Data from at least two independent experiments. (**C** and **D**). Effects of IL-33 administration to 8- to 12-week-old B6 males. Frequency (top) and numbers (bottom) of total IL-33$^+$ VmSCs (C) or of individual VmSC subtypes (D). Data shown correspond to at least two pooled independent experiments. Numbers of cells were tissue weight–normalized in all cases. *P < 0.05, **P < 0.01, ***P < 0.001, ****P < 0.0001. LFD, low-fat diet. All other statistics and abbreviations as per Figs. 1 and 5.

do in lean mice. An increase in IL-33 production upon HFD feeding is consistent with the observation that the pro-inflammatory cytokines IL-17 and tumor necrosis factor–α synergize to induce IL-33 expression by VAT stromal cells (*14*).

We have attempted to integrate the VmSC subtypes delineated herein with adipose tissue stromal cell populations recently defined on the basis of other scRNA-seq analyses. Schwalie *et al.* (*27*) exclusively studied iSAT rather than the eVAT depots we focused on. The "regulatory" subset they highlighted most closely resembles our VmSC3 subtype on the basis of marker transcript expression [e.g., *F3* (CD142) and *Abcg1*], low transcription of adipogenic genes (e.g., *Pparg*), and the inability to give rise to adipocytes in culture. However, it is dangerous to extrapolate between depots in this manner, as was also pointed out in the study of Burl *et al.* (*28*). Our total VmSC constellation appears to correspond to what these latter authors termed "adipocyte stem cells," defined by the expression of PDGFRα. They also found heterogeneity within this grouping but did not split it into its immunocyte-promoting and adipocyte-generating steady-state components, instead concentrating on adipocyte beiging.

Also notable is the identification of mesothelial stromal cells as IL-33 expressers. Mesothelial cells form a cobblestone monolayer surrounding organs in the peritoneal, pleural, and pericardial cavities, constituting a protective layer against physical damage (*29*). Hence, these cells would be well placed to exert IL-33's well-established alarmin function (*30*). In the VAT context, one can imagine a rheostat role wherein normal expansion of the fat pad (as happens with aging, for example) would induce expression of IL-33, a mechanosensitive cytokine (*31*), in turn prompting an increase in the VAT T_{reg} and ILC2 populations, and thereby keeping local inflammation in check. SAT is not surrounded by a layer of mesothelium (*15*), perhaps explaining the relatively paltry IL-33 and T_{reg} levels in these depots (*9*). Whether mesothelium surrounding other organs produces IL-33 to promote adaptive (T_{regs}) or innate (ILC2s) immune system surveillance of tissue homeostasis remains to be determined, but analogies in lung stromal cell compartments (*20*) suggest so.

An obvious question is how these observations relate to human adipose tissue. There are Foxp3-expressing cells in human omVAT,

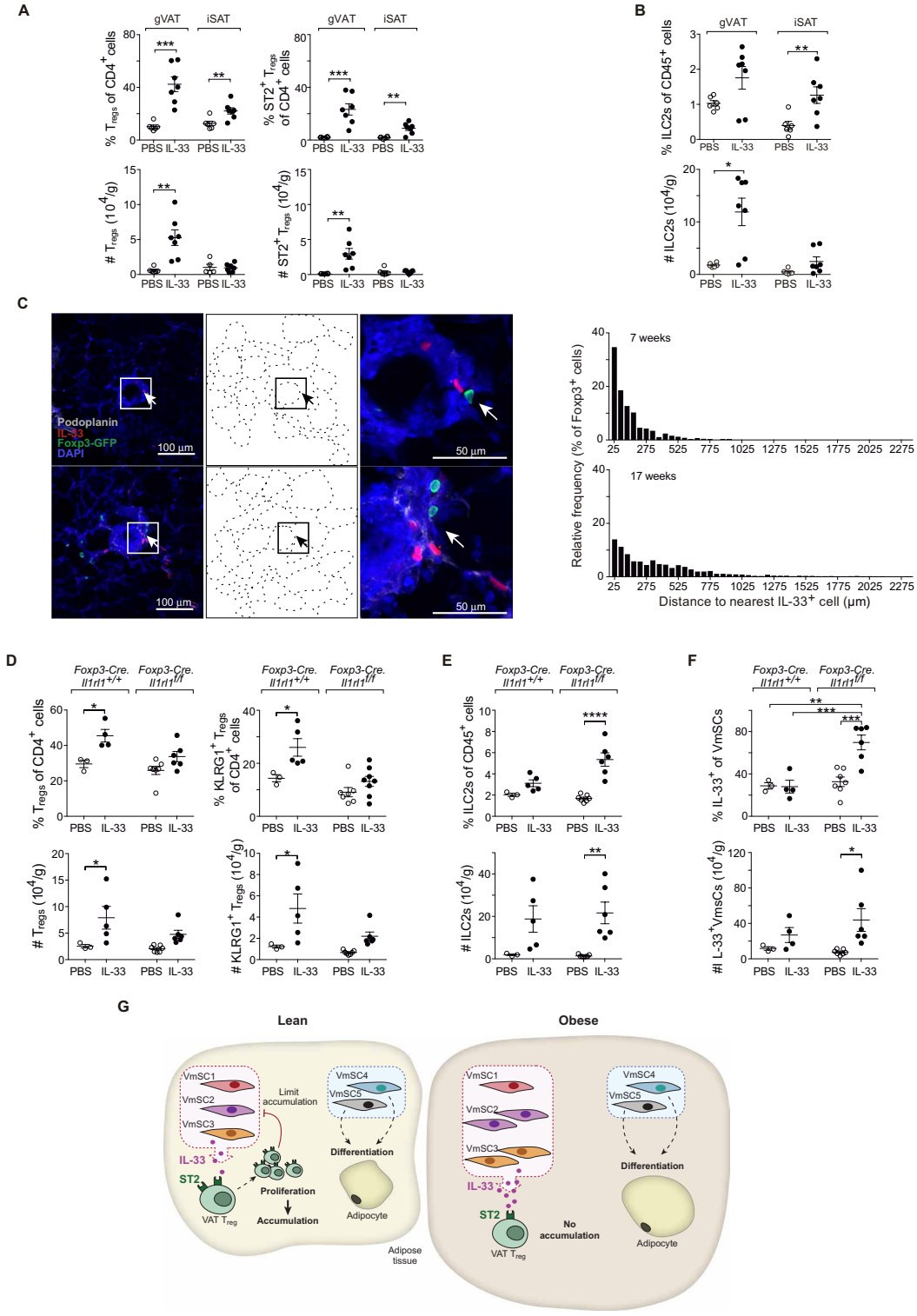

Fig. 8. Specific ST2 expression on VAT T_{regs} is involved in their interaction with VmSC subtypes. (**A** and **B**) IL-33 was administered to wild-type B6 males aged 8 to 12 weeks. Frequencies (top) and numbers (bottom) of total (left) and $ST2^+$ (right) T_{regs} (A) or ILC2s (B). (**C**) Confocal images (group of left panels) showing T_{regs} and IL-33–expressing cells within eVAT at low magnification (left), corresponding delineation of adipocyte edges based on autofluorescence of DAPI channel (middle), and high magnification of the squared indicated area (right). Distance quantification between $Foxp3^+$ T_{regs} and the nearest IL-33–expressing cell (group of right panels) from whole eVAT tissue sections taken from male VAT T_{reg} TCR-transgenic mice at 7 (top) and 17 (bottom) weeks of age. Arrows in (C) depict T_{reg}:$IL\text{-}33^+$ cell proximity. Color code for Ab staining as indicated within the picture. (**D** to **F**) IL-33 was injected into mice lacking ST2 expression specifically by T_{regs} versus wild-type littermate controls. Frequencies (top) and numbers (bottom) corresponding to total and $KLRG1^+$ T_{regs} (D), ILC2s (E), and $IL\text{-}33^+$ VmSCs (F). All numbers were calculated relative to total tissue weight. $^*P < 0.05$, $^{**}P < 0.01$, $^{***}P < 0.001$, $^{****}P < 0.0001$. (**G**) Graphic scheme of the proposed VmSC:T_{reg} negative regulatory loop model. All other abbreviations and statistics as per Figs. 1, 5, and 7.

fewer in obese than in lean individuals (*5*). T_{regs} in human VAT, but not blood, express ST2 (*7*). Human omVAT has a stromal cell population very similar to the $PDGFR\alpha^+$ IL-33–producing compartment in mice (*13*, *23*). Thus, it is likely that our observations will prove true, to at least some degree, in humans as well.

MATERIALS AND METHODS

Study design

The aims of this study were to identify and further characterize the cellular sources of IL-33 within VAT and to determine how these cells correlate with local T_{regs} in diverse physiologic and pathologic states.

We performed flow cytometric and confocal imaging experiments to detect IL-33–producing cells, followed by extensive transcriptional profiling at the single-cell population levels, in addition to functional characterization. We studied the abundance and phenotype of IL-33$^+$ subpopulations and T_{regs} in lean mice of different ages and sexes as well as in obesity.

Mice

C57BL/6 (B6) and C57BL/6-Tg(Pdgfra-Cre)1Clc/J (*Pdgfra-Cre*) (*32*) mice were obtained from the Jackson Laboratory. *Il1rl1*$^{-/-}$ (*33*) and *Il33*^{flox} (*34*) mice were donated by R. Lee (Brigham and Women's Hospital); B6(129S4)-*Il33*$^{tm1.1Bryc}$/J (*Il33*^{Egfp}) mice were donated by P. Bryce (Northwestern University) [now commercially available at Jackson (stock number 30619)]; *Foxp3-IRES-Gfp* (*35*), *Il33*$^{-/-}$, and *Il1rl1*^{flox} mice were donated by V. Kuchroo (Brigham and Women's Hospital); and *Foxp3-CreYFP* mice (*36*) were donated by A. Rudensky (Memorial Sloan Kettering Cancer Center). The VAT T_{reg} T cell receptor (TCR)–transgenic (vT_{reg}53) and *Pparg*^{Tdt} lines were recently described (*9*). Mice lacking ST2 specifically in T_{regs} were generated by crossing the *Il1rl1*^{flox} and *Foxp3-CreYFP* lines, double-reporter *Pparg*^{Tdt}/*Il33*^{Egfp} mice were generated by crossing the *Pparg*^{Tdt} and *Il33*^{Egfp} lines, and mice lacking IL-33 in mSCs were generated by mating the *Il33*^{flox} and *Pdgfra-Cre* lines. In all cases, mouse lines have been backcrossed to the B6 genetic background for at least eight generations, and experiments were conducted with littermate controls. All animals were housed at the specific pathogen–free facilities at Harvard Medical School (HMS). Experiments were performed under protocols approved by HMS's Institutional Animal Care and Use Committee (protocol #IS00001257). Except where otherwise noted, mice were fed a low-fat diet (no. 5053, Picolab Rodent Diet 20; 13% kcal fat per gram).

Preparation and flow cytometry of adipose tissue samples

Mice were euthanized using CO_2. eVAT, oVAT, omVAT, iSAT, and BAT were removed, placed into Dulbecco's modified Eagle's medium (DMEM) containing 2% fetal bovine serum (FBS), minced to mechanically disaggregate the tissue, and incubated with collagenase type II (1.5 mg/ml) (Sigma) at 37°C for 20 min with constant shaking in a water bath. Single-cell suspensions were washed with DMEM + 2% FBS, filtered through a 70-μm cell strainer, and further washed.

For flow cytometry involving surface staining only, cell preparations were subjected to red blood cell lysis by incubating with 0.5 to 1 ml ammonium-chloride-potassium lysing (ACK) buffer (Lonza) for 1 min on ice, washed, and finally resuspended in DMEM + 2% FBS for surface cytofluorimetric analysis. Staining with Abs recognizing CD45 (103125), CD31 (102406), Sca-1 (108124), PDGFRα (135908), and PDPN (127412) (all from BioLegend) was done for ~20 min at 4°C followed by LIVE/DEAD Fixable Near-Infrared viability dye (Thermo Fisher) incubation for 10 min at room temperature (RT). Following standard surface staining, intracellular IL-33 was detected by fixation and permeabilization using True-Nuclear Transcription Factor Buffer Set (BioLegend) as per the manufacturer's instructions followed by incubation with a goat anti–IL-33 polyclonal primary Ab (#AF326, R&D Systems) and a donkey anti-goat Cy3 secondary Ab (#705-166-147, Jackson Immunoresearch Laboratories). To delineate mSC subsets, we used anti-CD55 (#C62832, LSBio) and anti-Thy1 (#105326, BioLegend) Abs, whereas for T_{regs} and ILC2s, we employed a set of Abs directed against CD45 (#103126, BioLegend), CD4 (#100540, BioLegend), CD8 (#100706, BioLegend), ST2 (#25-9335-82, eBioscience), KRLG1 (#61-5893-82, Invitrogen), and CD25 (#102025, BioLegend), in addition to viability stain with LIVE/DEAD Fixable Yellow dye (Thermo Fisher). For staining of Foxp3, cell suspensions were fixed in eBioscience Fix/Perm buffer for 30 min at RT followed by permeabilization in eBioscience permeabilization buffer and overnight incubation at 4°C with anti-Foxp3 (#17-5773-82, eBioscience) and GATA3 (#12-9966-42, eBioscience). ILC2s were defined as CD45$^+$CD4$^-$CD8$^-$GATA3$^+$ST2$^+$/KLRG1$^+$ cells.

Confocal imaging of IL-33$^+$ cells

eVAT samples were fixed in 4% paraformaldehyde (PFA) (Electron Microscopy Sciences, PFA 16% solution, EM grade) for 24 hours and then treated with 30% sucrose solution for an additional 24 hours. Samples were then preserved in optimal cutting temperature (Tissue-Tek) and stored at −80°C until 100-μm sections were cut with a cryostat. For tissue staining, samples were blocked with 2% bovine serum albumin + 2% donkey serum + 0.5% Triton X-100 in phosphate-buffered saline (PBS) solution (immunofluorescence staining buffer) for 30 min, stained with primary Abs for 1 hour, and incubated in the presence of a secondary Ab for 30 min at RT. After each primary or secondary Ab staining, slides were washed three times for 5 min in PBS. Last, slides were mounted with Vectashield mounting medium (Vector Laboratories) or ProLong Diamond Antifade Mountant (Thermo Fisher). Primary Abs were goat anti-mouse IL-33 (#AF3526, 1:50 dilution; R&D Systems), allophycocyanin (APC)–conjugated Syrian Hamster anti-mouse PDPN (#AF3526, 1:100; BioLegend), or rabbit anti–green fluorescent protein (GFP) (1:1000, Abcam), rabbit anti–β3-tubulin (#D6584, 1:50; Cell Signaling), and rat anti-mouse CD31 (#102512, 1:50; BioLegend). Secondary Abs were Cy3 donkey anti-goat immunoglobulin G (IgG) (#705-166-147, 1:200; Jackson Immunoresearch Laboratories), Alexa Fluor 488 donkey anti-rabbit IgG (#406416, 1:200; BioLegend), or donkey anti-rat IgG (#712-175-153, Jackson Immunoresearch Laboratories). For β3-tubulin staining, eVAT from B6 retired breeder mice was used. Images were acquired on an Olympus FV1000 confocal microscope and were representative of at least three independent experiments.

PCR quantification

RNA was isolated from a <100-mg fragment of whole eVAT from the distal region using RNeasy Lipid Tissue Mini Kit (Qiagen) and reverse-transcribed using SuperScript Polymerase 2 (Invitrogen) according to the manufacturer's instructions. Real-time quantitative polymerase chain reaction (PCR) was performed using gene-specific fluorogenic assays (TaqMan; Applied Biosystems). Total Il33 transcript values were normalized to those from the mouse *Hprt* gene.

Three-dimensional spheroid in vitro culture of individually isolated VmSC subsets

eVAT from at least two mice was pooled, dispersed, and double-sorted using a Moflo Astrios cell sorter based on the VmSC markers mentioned above. Cells (2×10^3 to 2.5×10^3) were collected into a single well from a 384-well ultra-low attachment surface plate (Corning) containing 80 μl of DMEM/F12 GlutaMAX (Gibco), 10% FBS, penicillin-streptomycin, and Primocin. Cells were then spun down by centrifugation at 500*g* for 1 min and incubated in 5% CO_2 at 37°C. After 3 days, culture medium was carefully aspirated, and the cells were exposed to either DMEM/F12 GlutaMAX + 10% FBS and

penicillin-streptomycin (maintenance medium) or maintenance medium containing insulin from bovine pancreas (Sigma), 3-isobutyl-1-methylxanthine (Sigma), dexamethasone, and rosiglitazone (Cayman Chemical Company) for an additional 3 days. Cells were washed with PBS, fixed using 4% PFA for 10 min, and stained with HCS LipidTox Green (Thermo Fisher), which has affinity for neutral lipids, for 30 min at RT. Cells were left in Vectashield mounting medium with DAPI at 4°C until acquisition. Spheroids were visualized and imaged using an Olympus FV1000 confocal microscope. Serial pictures covering the spheroids separated by 4 μm from one another were taken, which were integrated into a single image using the Z-project function from ImageJ/Fiji software. Spheroid diameter was measured by tracing a line that covered the largest diameter.

Mouse manipulations

For the IL-33 administration experiments, 8- to 12-week-old B6, *Foxp3-Cre.Il1rl1*$^{+/+}$, or *Foxp3-Cre.Il1rl1*$^{fl/fl}$ male mice were intraperitoneally injected with either PBS or recombinant mouse IL-33 (BioLegend) at 2 μg per dose on days 0 and 3 and were analyzed on day 6. At 14 weeks of age, male B6 mice fed a low-fat diet containing 13% of its calories from fat (no. 5053, Picolab Rodent Diet 20) were either continued on this regimen (LFD group) or fed a HFD providing 60% of its calories from fat (Open Source Diet-D12492, irradiated) (HFD group) for 4 and 16 weeks. These mice underwent metabolic studies beginning at about 8 days before the end of the experiment, when a glucose tolerance test (GTT) was performed. Animals were fasted for an overnight period, weighed, and then evaluated for blood glucose concentrations at 0, 20, 40, 60, 90, and 120 min after intraperitoneal glucose administration (1.0 or 2.0 g/kg for short- or long-term experiments, respectively). The insulin tolerance test (ITT) was performed ~5 days after the GTT—in this case, mice were fasted for 4 hours and injected intraperitoneally with insulin (Humulin R, Lilly; 0.75 or 1.12 U/kg for short- or long-term experiments, respectively). Glucose concentrations were determined at 0, 20, 40, 60, 90, and 120 min afterward. For both GTTs and ITTs, the area under the curve was calculated using GraphPad Prism 7.0.

Quantification of T_{reg}:IL-33$^+$ cell distances

eVAT from 7- or 17-week-old male VAT T_{reg} TCR-transgenic mice expressing the Foxp3-GFP reporter (*9*) was stained as described above and imaged on an Olympus FV3000 confocal microscope using a 20× objective. Z-stack images of individual 20× fields were stitched together using Fluoview software (Olympus) to generate images of whole eVAT sections and were projected to obtain a two-dimensional image for quantification. For determination of the distance between IL-33$^+$ cells and T_{regs}, individual cells were identified using the Analyze Particle function in ImageJ/Fiji and manually verified. The coordinates of IL33$^+$ cells and T_{regs} (anti-GFP Ab staining) were obtained using the measurement function in Fiji, and the distances between these cells were calculated using a Euclidean distance formula. Quantifications were derived from 14 and 7 adipose tissue sections from mice aged 7 to 17 weeks, respectively.

Statistical analyses

Data were routinely shown as mean ± SEM. Unless stated otherwise, statistical significance was determined by the Student's *t* test or analysis of variance (ANOVA) using GraphPad Prism 7.0. *$P < 0.05$; **$P < 0.01$; ***$P < 0.001$; ****$P < 0.0001$. A value of more than three SDs from the mean was adopted as criteria to exclude outliers.

SUPPLEMENTARY MATERIALS

immunology.sciencemag.org/cgi/content/full/4/35/eaaw3658/DC1
Materials and Methods
Fig. S1. Controls for cytofluorimetric assessment of IL-33 expression.
Fig. S2. IL-33 expression primarily by mSCs is a common feature across male fat depots.
Fig. S3. *Pdgfra*-driven *Il33* ablation affects the amount of mature VAT T_{regs} without affecting body, fat depot weights, or VmSC quantities in young lean male mice.
Fig. S4. Intracellular anti–IL-33 staining is an alternative to IL-33 reporter fluorescence for VmSC subtype quantification.
Fig. S5. Distinct gene expression profiles of VmSC subsets reveal functional heterogeneity.
Fig. S6. Aging affects VAT T_{regs}, weights, and VmSCs.
Fig. S7. Gender-specific differences in T_{regs}.
Fig. S8. VmSCs constitute the main source of IL-33 in different adipose depot in females.
Fig. S9. Diet-induced obesity provokes VAT T_{reg} loss and VmSC remodeling.
Fig. S10. Specific IL-33 sensing by VAT T_{regs} alters VmSC dynamics.
Table S1. Specific and shared gene clusters reveal VmSC subsets' heterogeneity.
Table S2. Overrepresented pathways of VmSC subsets from 8-week-old male mice.
Table S3. Cardinal gene expression profiles in VmSC subsets.
Table S4. Differential expression of extracellular matrix and soluble protein on VmSC subtypes.
Table S5. GSEA of VmSC subsets from female vis-à-vis male mice aged 8 to 10 weeks.
Table S6. Raw data.
References (*37*–*46*)

REFERENCES AND NOTES

1. G. S. Hotamisligil, Foundations of immunometabolism and implications for metabolic health and disease. *Immunity* **47**, 406–420 (2017).
2. Y. S. Lee, J. Wollam, J. M. Olefsky, An integrated view of immunometabolism. *Cell* **172**, 22–40 (2018).
3. S. P. Weisberg, D. McCann, M. Desai, M. Rosenbaum, R. L. Leibel, A. W. Ferrante Jr., Obesity is associated with macrophage accumulation in adipose tissue. *J. Clin. Invest.* **112**, 1796–1808 (2003).
4. H. Xu, G. T. Barnes, Q. Yang, G. Tan, D. Yang, C. J. Chou, J. Sole, A. Nichols, J. S. Ross, L. A. Tartaglia, H. Chen, Chronic inflammation in fat plays a crucial role in the development of obesity-related insulin resistance. *J. Clin. Invest.* **112**, 1821–1830 (2003).
5. M. Feuerer, L. Herrero, D. Cipolletta, A. Naaz, J. Wong, A. Nayer, J. Lee, A. B. Goldfine, C. Benoist, S. Shoelson, D. Mathis, Lean, but not obese, fat is enriched for a unique population of regulatory T cells that affect metabolic parameters. *Nat. Med.* **15**, 930–939 (2009).
6. A. B. Molofsky, J. C. Nussbaum, H.-E. Liang, S. J. Van Dyken, L. E. Cheng, A. Mohapatra, A. Chawla, R. M. Locksley, Innate lymphoid type 2 cells sustain visceral adipose tissue eosinophils and alternatively activated macrophages. *J. Exp. Med.* **210**, 535–549 (2013).
7. A. Vasanthakumar, K. Moro, A. Xin, Y. Liao, R. Gloury, S. Kawamoto, S. Fagarasan, L. A. Mielke, S. Afshar-Sterle, S. L. Masters, S. Nakae, H. Saito, J. M. Wentworth, P. Li, W. Liao, W. J. Leonard, G. K. Smyth, W. Shi, S. L. Nutt, S. Koyasu, A. Kallies, The transcriptional regulators IRF4, BATF and IL-33 orchestrate development and maintenance of adipose tissue-resident regulatory T cells. *Nat. Immunol.* **16**, 276–285 (2015).
8. D. Kolodin, P. N. van, C. Li, A. M. Magnuson, D. Cipolletta, C. M. Miller, A. Wagers, R. N. Germain, C. Benoist, D. Mathis, Antigen- and cytokine-driven accumulation of regulatory T cells in visceral adipose tissue of lean mice. *Cell Metab.* **21**, 543–557 (2015).
9. C. Li, J. R. Dispirito, D. Zemmour, R. G. Spallanzani, W. Kuswanto, C. Benoist, D. Mathis, TCR transgenic mice reveal stepwise, multi-site acquisition of the distinctive fat-Treg phenotype. *Cell* **174**, 285–299.e12 (2018).
10. A. B. Molofsky, G. F. Van, H. E. Liang, S. J. Van Dyken, J. C. Nussbaum, J. Lee, J. A. Bluestone, R. M. Locksley, Interleukin-33 and interferon-γ counter-regulate group 2 innate lymphoid cell activation during immune perturbation. *Immunity* **43**, 161–174 (2015).
11. D. Burzyn, W. Kuswanto, D. Kolodin, J. L. Shadrach, M. Cerletti, Y. Jang, E. Sefik, T. G. Tan, A. J. Wagers, C. Benoist, D. Mathis, A special population of regulatory T cells potentiates muscle repair. *Cell* **155**, 1282–1295 (2013).
12. T. Y. F. Halim, B. M. J. Rana, J. A. Walker, B. Kerscher, M. D. Knolle, H. E. Jolin, E. M. Serrao, L. Haim-Vilmovsky, S. A. Teichmann, H. R. Rodewald, M. Botto, T. J. Vyse, P. G. Fallon, Z. Li, D. R. Withers, A. N. J. McKenzie, Tissue-restricted adaptive type 2 immunity is orchestrated by expression of the costimulatory molecule OX40L on group 2 innate lymphoid cells. *Immunity* **48**, 1195–1207.e6 (2018).
13. S. K. Chang, A. C. Kohlgruber, F. Mizoguchi, X. Michelet, B. J. Wolf, K. Wei, P. Y. Lee, L. Lynch, D. Duquette, V. Ceperuelo-Mallafre, A. S. Banks, M. B. Brenner, Stromal cell cadherin-11 regulates adipose tissue inflammation and diabetes. *J. Clin. Invest.* **127**, 3300–3312 (2017).
14. A. C. Kohlgruber, S. T. Gal-Oz, N. M. LaMarche, M. Shimazaki, D. Duquette, H.-F. Koay, H. N. Nguyen, A. I. Mina, T. Paras, A. Tavakkoli, A. U. von, A. S. Banks, T. Shay, M. B. Brenner, L. Lynch, γδ T cells producing interleukin-17A regulate adipose regulatory T cell homeostasis and thermogenesis. *Nat. Immunol.* **19**, 464–474 (2018).

15. O. T. Gupta, R. K. Gupta, Visceral adipose tissue mesothelial cells: Living on the edge or just taking up space? *Trends Endocrinol. Metab.* **26**, 515–523 (2015).
16. M. Pichery, E. Mirey, P. Mercier, E. Lefrancais, A. Dujardin, N. Ortega, J.-P. Girard, Endogenous IL-33 is highly expressed in mouse epithelial barrier tissues, lymphoid organs, brain, embryos, and inflamed tissues: In situ analysis using a novel Il-33-LacZ gene trap reporter strain. *J. Immunol.* **188**, 3488–3495 (2012).
17. M. E. Bernardo, W. E. Fibbe, Mesenchymal stromal cells: Sensors and switchers of inflammation. *Cell Stem Cell* **13**, 392–402 (2013).
18. R. Zilionis, J. Nainys, A. Veres, V. Savova, D. Zemmour, A. M. Klein, L. Mazutis, Single-cell barcoding and sequencing using droplet microfluidics. *Nat. Protoc.* **12**, 44–73 (2017).
19. M. G. La, R. Soldatov, A. Zeisel, E. Braun, H. Hochgerner, V. Petukhov, K. Lidschreiber, M. E. Kastriti, P. Lönnerberg, A. Furlan, J. Fan, L. E. Borm, Z. Liu, B. D. van, J. Guo, X. He, R. Barker, E. Sundström, G. Castelo-Branco, P. Cramer, I. Adameyko, S. Linnarsson, P. V. Kharchenko, RNA velocity of single cells. *Nature* **560**, 494–498 (2018).
20. T. Xie, Y. Wang, N. Deng, G. Huang, F. Taghavifar, Y. Geng, N. Liu, V. Kulur, C. Yao, P. Chen, Z. Liu, B. Stripp, J. Tang, J. Liang, P. W. Noble, D. Jiang, Single-cell deconvolution of fibroblast heterogeneity in mouse pulmonary fibrosis. *Cell Rep.* **22**, 3625–3640 (2018).
21. L. Vishvanath, K. A. MacPherson, C. Hepler, Q. A. Wang, M. Shao, S. B. Spurgin, M. Y. Wang, C. M. Kusminski, T. S. Morley, R. K. Gupta, Pdgfrβ^{+} mural preadipocytes contribute to adipocyte hyperplasia induced by high-fat diet feeding and prolonged cold exposure in adult mice. *Cell Metab.* **23**, 350–359 (2016).
22. D. Cipolletta, P. Cohen, B. M. Spiegelman, C. Benoist, D. Mathis, Appearance and disappearance of the mRNA signature characteristic of T_{reg} cells in visceral adipose tissue: Age, diet, and PPARγ effects. *Proc. Natl. Acad. Sci. U.S.A.* **112**, 482–487 (2015).
23. G. Marcelin, A. Ferreira, Y. Liu, M. Atlan, J. Aron-Wisnewsky, V. Pelloux, Y. Botbol, M. Ambrosini, M. Fradet, C. Rouault, C. Hénégar, J. S. Hulot, C. Poitou, A. Torcivia, R. Nail-Barthelemy, J. C. Bichet, E. L. Gautier, K. Clément, A PDGFRα-mediated switch toward CD9^{high} adipocyte progenitors controls obesity-induced adipose tissue fibrosis. *Cell Metab.* **25**, 673–685 (2017).
24. D. Cipolletta, M. Feuerer, A. Li, N. Kamei, J. Lee, S. E. Shoelson, C. Benoist, D. Mathis, PPAR-γ is a major driver of the accumulation and phenotype of adipose tissue T_{reg} cells. *Nature* **486**, 549–553 (2012).
25. T. Mahlakõiv, A.-L. Flamar, L. K. Johnston, S. Moriyama, G. G. Putzel, P. J. Bryce, D. Artis, Stromal cells maintain immune cell homeostasis in adipose tissue via production of interleukin-33. *Sci. Immunol.* **4**, eaax0416 (2019).
26. S. J. Han, Z. A. Glatman, V. Andrade-Oliveira, N. Collins, A. Dzutsev, J. Shaik, F. D. Morais da Fonseca, O. J. Harrison, S. Tamoutounour, A. L. Byrd, M. Smelkinson, N. Bouladoux, J. B. Bliska, J. M. Brenchley, I. E. Brodsky, Y. Belkaid, White adipose tissue is a reservoir for memory T cells and promotes protective memory responses to infection. *Immunity* **47**, 1154–1168.e6 (2017).
27. P. C. Schwalie, H. Dong, M. Zachara, J. Russeil, D. Alpern, N. Akchiche, C. Caprara, W. Sun, K.-U. Schlaudraff, G. Soldati, C. Wolfrum, B. Deplancke, A stromal cell population that inhibits adipogenesis in mammalian fat depots. *Nature* **559**, 103–108 (2018).
28. R. B. Burl, V. D. Ramseyer, E. A. Rondini, R. Pique-Regi, Y. H. Lee, J. G. Granneman, Deconstructing adipogenesis induced by β3-adrenergic receptor activation with single-cell expression profiling. *Cell Metab.* **28**, 300–309.e4 (2018).
29. S. E. Mutsaers, The mesothelial cell. *Int. J. Biochem. Cell Biol.* **36**, 9–16 (2004).
30. N. T. Martin, M. U. Martin, Interleukin 33 is a guardian of barriers and a local alarmin. *Nat. Immunol.* **17**, 122–131 (2016).
31. R. Kakkar, H. Hei, S. Dobner, R. T. Lee, Interleukin 33 as a mechanically responsive cytokine secreted by living cells. *J. Biol. Chem.* **287**, 6941–6948 (2012).
32. K. Roesch, A. P. Jadhav, J. M. Trimarchi, M. B. Stadler, B. Roska, B. B. Sun, C. L. Cepko, The transcriptome of retinal Müller glial cells. *J. Comp. Neurol.* **509**, 225–238 (2008).
33. M. J. Townsend, P. G. Fallon, D. J. Matthews, H. E. Jolin, A. N. J. McKenzie, T1/ST2-deficient mice demonstrate the importance of T1/ST2 in developing primary T helper cell type 2 responses. *J. Exp. Med.* **191**, 1069–1076 (2000).
34. W.-Y. Chen, J. Hong, J. Gannon, R. Kakkar, R. T. Lee, Myocardial pressure overload induces systemic inflammation through endothelial cell IL-33. *Proc. Natl. Acad. Sci. U.S.A.* **112**, 7249–7254 (2015).
35. E. Bettelli, Y. Carrier, W. Gao, T. Korn, T. B. Strom, M. Oukka, H. L. Weiner, V. K. Kuchroo, Reciprocal developmental pathways for the generation of pathogenic effector T_H17 and regulatory T cells. *Nature* **441**, 235–238 (2006).
36. Y. P. Rubtsov, J. P. Rasmussen, E. Y. Chi, J. Fontenot, L. Castelli, X. Ye, P. Treuting, L. Siewe, A. Roers, W. R. Henderson Jr., W. Muller, A. Y. Rudensky, Regulatory T cell-derived interleukin-10 limits inflammation at environmental interfaces. *Immunity* **28**, 546–558 (2008).
37. D. Zemmour, R. Zilionis, E. Kiner, A. M. Klein, D. Mathis, C. Benoist, Single-cell gene expression reveals a landscape of regulatory T cell phenotypes shaped by the TCR. *Nat. Immunol.* **19**, 291–301 (2018).
38. D. Kim, G. Pertea, C. Trapnell, H. Pimentel, R. Kelley, S. L. Salzberg, TopHat2: Accurate alignment of transcriptomes in the presence of insertions, deletions and gene fusions. *Genome Biol.* **14**, R36 (2013).
39. L. van der Maaten, G. Hinton, Visualizing high-dimensional data using t-SNE. *J. Mach. Learn. Res.* **9**, 2579–2605 (2008).
40. A. M. Klein, L. Mazutis, I. Akartuna, N. Tallapragada, A. Veres, V. Li, L. Peshkin, D. A. Weitz, M. W. Kirschner, Droplet barcoding for single-cell transcriptomics applied to embryonic stem cells. *Cell* **161**, 1187–1201 (2015).
41. D. Grün, A. Lyubimova, L. Kester, K. Wiebrands, O. Basak, N. Sasaki, H. Clevers, O. A. van, Single-cell messenger RNA sequencing reveals rare intestinal cell types. *Nature* **525**, 251–255 (2015).
42. R Development Core Team, R: A language and environment for statistical computing. Vienna, Austria: The R Foundation for Statistical Computing (2017); http://www.R-project.org.
43. M. I. Love, W. Huber, S. Anders, Moderated estimation of fold change and dispersion for RNA-seq data with DESeq2. *Genome Biol.* **15**, 550 (2014).
44. S. Picelli, O. R. Faridani, A. K. Björklund, G. Winberg, S. Sagasser, R. Sandberg, Full-length RNA-seq from single cells using Smart-seq2. *Nat. Protoc.* **9**, 171–181 (2014).
45. C. Trapnell, A. Roberts, L. Goff, G. Pertea, D. Kim, D. R. Kelley, H. Pimentel, S. L. Salzberg, J. L. Rinn, L. Pachter, Differential gene and transcript expression analysis of RNA-seq experiments with TopHat and Cufflinks. *Nat. Protoc.* **7**, 562–578 (2012).
46. A. Subramanian, P. Tamayo, V. K. Mootha, S. Mukherjee, B. L. Ebert, M. A. Gillette, A. Paulovich, S. L. Pomeroy, T. R. Golub, E. S. Lander, J. P. Mesirov, Gene set enrichment analysis: A knowledge-based approach for interpreting genome-wide expression profiles. *Proc. Natl. Acad. Sci. U.S.A.* **102**, 15545–15550 (2005).

Acknowledgments: We thank V. Kuchroo, R. Lee, A. Rudensky, and A. McKenzie for providing mice; A. Ortiz-Lopez, K. Hattori, N. Asinovski, A. Rhoads, K. Seddu, A. Cook, G. Buruzula, C. Araneo, A. Wood, and F. Lopez for experimental assistance; C. Laplace for graphic design support; and B. Spiegelman for discussions. Cell sorting was performed at the HSCI/DRC Flow Core of the Joslin Diabetes Center (NIH P30 DK036836), and InDrops was done at the HMS Single Cell Core. P.J.B. generated the IL-33 conditional reporter mouse line while an employee at Northwestern University but is currently an employee of Sanofi US, which was not involved in this study. **Funding:** This work was supported by NIH grants DK092451, RC2DK116691, AR080334 and by a grant from the JPB Foundation and a Dean's Innovation Grant to D.M. R.G.S. is an American Diabetes Association Postdoctoral fellow (1-17-PMF-005). D.Z. was supported by a fellowship from the Boehringer Ingelheim Fonds, T.J. was supported by NIH Training Grant T32GM007753, and C.L. was supported by a Cancer Research Institute Irvington fellowship. **Author contributions:** R.G.S., D.Z., T.X., T.J., and C.L. designed and performed experiments, conducted statistical analyses, and analyzed the data together with C.B. and D.M. R.G.S. and D.M. wrote the manuscript, which all authors edited. **Competing interests:** The authors declare that they have no competing interests. **Data and materials availability:** ScRNA-seq datasets from VAT, muscle, and lymph node mesenchymal stromal cells along with population-level RNA-seq of individual VmSC subsets from both male and female mice aged 8 to 10 weeks old were deposited in Gene Expression Omnibus under accession numbers GSE127005 and GSE126891, respectively. All other data needed to evaluate the conclusions in the paper are present in the paper or the Supplementary Materials.

Submitted 12 December 2018
Accepted 6 March 2019
Published 3 May 2019
10.1126/sciimmunol.aaw3658

Citation: R. G. Spallanzani, D. Zemmour, T. Xiao, T. Jayewickreme, C. Li, P. J. Bryce, C. Benoist, D. Mathis, Distinct immunocyte-promoting and adipocyte-generating stromal components coordinate adipose tissue immune and metabolic tenors. *Sci. Immunol.* **4**, eaaw3658 (2019).

Science Immunology

Distinct immunocyte-promoting and adipocyte-generating stromal components coordinate adipose tissue immune and metabolic tenors

Raul German Spallanzani, David Zemmour, Tianli Xiao, Teshika Jayewickreme, Chaoran Li, Paul J. Bryce, Christophe Benoist and Diane Mathis

Sci. Immunol. **4**, eaaw3658.
DOI: 10.1126/sciimmunol.aaw3658

Stromal sources of IL-33 in fat depots

White adipose tissue (WAT) is home to T_{regs} and group 2 innate lymphoid cells (ILC2s) that help keep inflammation under check. Two studies in this week's issue probe WAT in search of cells producing the alarmin cytokine IL-33 that regulates T_{regs} and ILC2s. Spallanzani *et al*. used single-cell RNA sequencing to characterize visceral WAT stromal cells and defined five distinct subtypes, with subtypes 1 to 3 producing IL-33 and subtypes 4 and 5 resembling adipocyte precursors. Mahlakõiv *et al*. identified adipose stem and progenitor cells as a source of IL-33 in all WAT depots and mesothelial cells as an additional source of IL-33 in visceral WAT. These studies improve our understanding of WAT stromal cell diversity and how the stromal cell landscape responds to physiological or pathological variations. See the related Research Article by Mahlakõiv *et al*.